NeuroImage 57 (2011) 452–461

Contents lists available at ScienceDirect

NeuroImage

journal homepage: www.elsevier.com/locate/ynimg

# Susceptibility phase imaging with comparison to R2* mapping of iron-rich deep grey matter

Andrew J. Walsh, Alan H. Wilman *

*Department of Biomedical Engineering, University of Alberta, Edmonton, Alberta, Canada T6G 2V2*

ARTICLE INFO

*Article history:*
Received 24 December 2010
Revised 30 March 2011
Accepted 7 April 2011
Available online 13 April 2011

*Keywords:*
Phase
Susceptibility
Iron
Phase filtering
R2* mapping
T2*

ABSTRACT

Magnetic resonance imaging with susceptibility phase is seeing increasing use, especially at high magnetic fields. Tissue susceptibility can produce unique phase contrast for qualitative or quantitative imaging of iron-rich deep grey matter. However, phase imaging has several established sources of error including inherent susceptibility field effects and artifacts from background phase removal. These artifacts have led to inconsistent findings in past works relating iron to phase in healthy deep grey matter. This study seeks to determine the relative artifactual contributions from inherent susceptibility fields and from high pass phase filtering, currently the most common and accessible background phase removal method. In simulation, phase is compared to a known susceptibility distribution, while R2* maps are used as the in vivo gold standard surrogate for iron in healthy volunteers. The results indicate phase imaging depends highly on filtering, structure size, shape and local environment. Using in vivo phase and R2* profiles, it is shown that different filtering values, commonly seen in the literature, can lead to substantially different phase measures. Correlations between phase and R2* mapping are shown to be highly variable between structures. For example, using a standard filter of 0.125 the slopes and correlation coefficients were $4.28\times10^{-4}$ ppm*s and $R=0.88$ for the putamen, $0.81\times10^{-4}$ ppm*s and $R=0.08$ for the globus pallidus, $5.48\times10^{-4}$ ppm*s and $R=0.72$ for the red nucleus, and $-14.64\times10^{-4}$ ppm*s and $R=0.54$ for the substantia nigra. To achieve the most effective correlation to R2* we recommend using a filter width of 0.094 for the globus pallidus and putamen and 0.125 for the substantia nigra and red nucleus. The baseline phase measure should be obtained directly adjacent to the substantia nigra, and red nucleus to yield the most accurate phase values as demonstrated in simulation and in vivo. Different regression slopes are seen between subROIs within structures suggesting that regional iron accumulation within a structure is best studied with subROIs between different subject groups, not differences in phase values relative to the overall phase in one structure. Phase imaging with the standard high pass filter method has the potential to differentiate subtle iron changes in pathological processes compared to normal tissues with more reliability if specific filter strengths and measurement areas are appropriately applied on a structure dependent basis.



## Introduction

Phase susceptibility imaging and susceptibility-weighted imaging (SWI) have demonstrated sensitivity to brain iron (Haacke et al., 2004; Ogg et al., 1999), which has been shown to accumulate in neurodegenerative diseases such as Alzheimer's disease (Bartzokis and Tishler, 2000), Parkinson's disease (Baudrexel et al., 2010), and multiple sclerosis (MS) (Pinero and Connor, 2000). These imaging methods have been used for quantifying iron changes in deep grey matter (Haacke et al., 2009a; Ogg et al., 1999) and qualitatively for enhancing image contrast, particularly between MS lesions and normal tissue (Eissa et al., 2009; Haacke et al., 2009b; Hammond et al., 2008b). While transverse relaxation rate (R2 or R2*) mapping is sensitive to iron in normal individuals (Bermel et al., 2005), phase imaging should be both more sensitive to iron because it depends on subtle phase shifts rather than significant dephasing, and more specific since phase is not significantly affected by water content, which could be a confound in cases of neurodegeneration (Mitsumori et al., 2009).

Putative quantitative iron measures are seeing increasing use with phase imaging (Hammond et al., 2008b; Hopp et al., 2010; Xu et al., 2008), however, studies have not shown consistent reliability of phase imaging for iron measurement because phase is also confounded by certain physical factors including: the angle of brain structure to the Bo field (Schafer et al., 2009), neuronal fiber orientation (Lee et al., 2010b), myelin content (Duyn et al., 2007), calcium and phospholipid content (He and Yablonskiy, 2009), neighboring susceptibility sources (Wharton and Bowtell, 2010), and the type of background phase removal method (Haacke et al., 2004; Neelavalli et al., 2009; Wharton and Bowtell, 2010; Yao et al., 2009). By focusing on the iron-rich basal

* Corresponding author at: 1098 RTF, Department of Biomedical Engineering, University of Alberta Edmonton, Alberta, Canada T6G 2V2. Fax: +1 780 492 8259.
*E-mail address:* alan.wilman@ualberta.ca (A.H. Wilman).

1053-8119/$ – see front matter © 2011 Elsevier Inc. All rights reserved.
doi:10.1016/j.neuroimage.2011.04.017

ganglia, where there are substantial deposits of non-heme iron, factors such as phospholipids, myelin and fiber orientation will contribute a smaller role bringing background phase removal and susceptibility field effects to the forefront.

Background phase removal is necessary to remove the global magnetic field variations created by the geometry of the head and air tissue interfaces, such as the nasal cavity, in order to provide access to the underlying field variations related to the local tissue environment. While new phase background removal methods are continually evolving, standard phase imaging with simple background phase removal through phase filtering has been used extensively throughout the short history of phase imaging (Haacke et al., 2007; Hopp et al., 2010; Wang et al., 2000) and in recent neurological studies (Gupta et al., 2010; Rossi et al., 2010; Szumowski et al., 2010; Zhang et al., 2010; Zhu et al., 2009). As well, the phase filtering approach has the advantage of being relatively easy to implement and is widely available on many clinical MRI systems. Although this method produces visually interpretable images, it can alter the true phase values in certain brain structures. The effect of filtering on phase images has implications in quantitative phase measurements because effects of filtering depend upon object shape and size. This requires an in-depth understanding of shape effects.

The effect of phase suppression from varying filter strength has been previously presented qualitatively (Hammond et al., 2008a), and quantitatively (Haacke et al., 2007; Pfefferbaum et al., 2009) which has led to one common standard filtering approach of utilizing ~12% of the image in a low pass filter, in order to suppress background global fields but attempt to retain local phase differences. The quantitative studies either did not examine deep grey matter or did not compare subsections of the structures between filter strengths. Since deep grey matter structures vary in shape and size, different parts of structures could be affected differently by filtering and this could have implications when examining iron accumulation patterns.

As well as phase filtering, susceptibility field effects also substantially affect phase images (de Rochefort et al., 2010; Deistung et al., 2008; Schafer et al., 2009). These dipolar field effects result from the susceptibility difference, $\Delta\chi$, between the inner and external environment of a structure and phase effects are produced within and around structures. Considering a very simple spherical susceptibility distribution, the analytical solution for field effect changes is well known depending on $\Delta\chi$ inside of the spherical structure, and outside on $\Delta\chi$ and on the directional component $3\cos^2(\theta)-1$, where $\theta$ is the angle to the main magnetic field. More geometrically complex susceptibility distributions require a numerical computation by multiplication of a dipole field in *k*-space (Schafer et al., 2009), which has demonstrated the directional, and nonlocal, field effects of more anatomically representative distributions.

In the human brain, R2* values have shown very high correlation to post mortem iron concentrations $r=0.9$ (Langkammer et al., 2010). However, previous studies have correlated phase or R2* to predicted iron content of the basal ganglia with minimal success (Haacke et al., 2010; Wharton and Bowtell, 2010; Yao et al., 2009). These studies compared phase between different structures in the same individual, while examining the same structure across individuals would enable phase-iron correlation without the confounding effects of structure dependent filtering and field shift due to structure shape.

In this work, phase imaging is compared to quantitative R2* mapping across multiple volunteers to demonstrate the role of susceptibility fields, phase filtering and ROI placement in each iron-rich, deep grey matter structure. Phase variations are examined in simulation and in vivo experiments using a wide range of filters with clear separation of susceptibility field effects from filter reconstruction effects. Structure-dependent recommendations for filter size and ROI placement are provided. By quantifying the possible confounds of phase imaging in deep grey matter, a means for better interpretation of quantitative phase imaging is provided.

## Materials and methods

Phase imaging was studied in three ways. First, a computer simulation tested the effects of phase filtering using a simple susceptibility model that accounted for inherent susceptibility fields. Second, in vivo phase susceptibility experiments were performed at 3.0 T on healthy subjects to validate simulation findings. Third, the in vivo phase susceptibility within each deep grey matter structure was measured using different filters and ROI placements, and correlated to corresponding R2* measurements.

### *Susceptibility field modeling*

A simplified 3D susceptibility distribution of the basal ganglia was created in Matlab (MathWorks Inc., Massachusetts, USA) using only the putamen (PUT), globus pallidus (GP), substantia nigra (SN), and red nucleus (RN). The model boundaries were traced from a healthy control subject using multiple axial slices (3 mm thick, TE 40 ms, gradient echo). Voxels inside each region received homogeneous susceptibility values (PUT = 0.09 ppm, GP = 0.18 ppm, SN = 0.16 ppm, RN = 0.13 ppm) based on values calculated by Wharton and Bowtell (2010). Voxels outside these regions were set to zero. These slices were interpolated to create a 3D volume with 0.5 mm isotropic pixel dimension. This 3D susceptibility distribution was Fourier transformed into *k*-space and multiplied by the corresponding dipole field using a field forward calculation as described in Marques and Bowtell (2005) and Salomir et al. (2003). The resulting *k*-space volume was then inverse Fourier transformed to produce a field map in image space. Three planes in the z direction were then averaged to produce 1.5 mm thick slices for 2D filtering.

### *Filter*

The phase image resulting from the field effects of the model was subject to 2D spatial high pass filtering with increasing strength of filters. The standard filtering method of Haacke was used (Haacke et al., 2009b; Wang et al., 2000). A 2D symmetrical Hanning window was constructed in *k*-space, size m × m points, and zero padded to the full $n \times n$ matrix size, of the original 2D image. The filter width was defined as the ratio of one dimension of the Hanning window divided by the total filter size in that dimension: $m/n$, using a square field of view and isotropic resolution. A typical filter reported is 0.125 filter width or greater (Pfefferbaum et al., 2009; Wang et al., 2000). Filtering effects were examined using a range of filter widths from 0 to 0.2. The raw *k*-space data matrix was multiplied by this 2D Hanning window, and the result was Fourier transformed to the spatial domain, resulting in a low pass filtered image. This low pass image was complex divided into the original image to produce a high pass filtered image from which phase angles were calculated.

### *Phase behavior in simulation*

The simulated 2D images of the GP-PUT and SN-RN slices were examined with 4 different filter widths (0.063, 0.094, 0.125, and 0.200) and compared to images of the raw phase and the susceptibility distribution. The effects arising from filtering and from field shifts were studied. Next, the field effect created by neighboring susceptibility distributions was examined more closely by assigning a constant susceptibility to the GP (0.16 ppm) with four different susceptibility values assigned to the PUT (0.06, 0.09, 0.12, 0.15 ppm). These four separate simulations were filtered with the standard 0.125 filter width to illustrate the internal phase effects in a brain structure from external susceptibility sources within neighboring tissue, while using a constant filter. Conversely, the internal phase within the SN due to inherent susceptibility was studied by assigning susceptibility

values to the SN (0.18, 0.16, 0.14 ppm). The effect of external field shifts caused by the different susceptibility values assigned to the PUT within the GP were studied by comparing the cross sectional profiles though both structures. The phase within the SN due to different susceptibility values from within the structure was studied by comparing the measured phase to the assigned susceptibility from ROIs which encompass the entire 2D structure in one axial image.

To quantify the phase effect due to structure shape and filter strength, measures from a cross sectional profile of the deep grey matter structures were obtained in simulation. To compare simulation to in vivo measures, fractional measures were used to remove the effects of varying structure susceptibility across subjects. Phase changes were evaluated by comparing the edge phase to middle phase values between filters, and the change in edge phase between filters.

To evaluate the phase changes across a structure with different filter widths, the measures between phase at the edge minus the middle divided by the edge minus the baseline produced a fractional phase change from the edge to middle of the structure. The baseline was measured adjacent to the outside edge of the structure. For normalization, the divisor (const) was based on the measured phase from the smallest filter width profile and the edge to middle phase was compared between four filter widths (0.200, 0.125, 0.094 0.063).

$$\text{Phase change middle}_i = (\text{edge}_i - \text{middle}_i) / (\text{edge}_{const} - \text{base}_{const}) \quad (1)$$

Also of interest are the changes in edge phase with the four different filter widths between the simulated structures. The phase measured at the edge subtracted from the baseline phase of a structure with one of the four filter widths was subtracted from the edge phase subtracted from the baseline phase using the smallest filter width. The result was divided by the phase measured at the edge subtracted by the phase measured at the base immediately outside of the structure with the smallest filter width.

$$\text{Phase change edge}_i = [(\text{edge}_i - \text{base}_i) - (\text{edge}_{const} - \text{base}_{const})] / (\text{edge}_{const} - \text{base}_{const}) \quad (2)$$

In Eqs. (1) and (2), the constant, or smallest filter width, for edge and base is 0.094 for the RN and SN and 0.063 for the GP and PUT. The 0.063 filter width was not used to evaluate the SN and RN because of visible phase wrapping within these structures in vivo when this small filter width was applied.

*Volunteer MRI acquisition*

Images were obtained from seven healthy volunteers (age 36 ± 16 years) to quantify the effects of filter width on the phase measured within deep grey matter structures and to correlate R2* to phase. Using a 3.0 T MRI system, a 2D gradient echo sequence (flip angle 60°, TR 500 ms, 512 frequency × 256 phase, 3 mm thickness, 7 slices, no slice separation, FOV 25 cm) was used to image the basal ganglia. The images were zero padded in *k*-space to 512 × 512 resolution before phase filtering. Four separate echo times were used TE 9/16/26/40 ms (Du et al., 2009) with 40 ms being the maximum because images acquired with a greater TE incurred artifact from field inhomogeneities due to the nasal cavity and paranasal sinuses. R2* maps of the brain were obtained by fitting the four echoes with a single exponential decay. R2* values from structures in the basal ganglia were compared to the phase values computed from the TE = 16 ms and 26 ms images since typically phase images are acquired at TE of 16–26 ms at 3.0 T (Denk and Rauscher, 2010; Lee et al., 2010a). Four filter widths were applied to each image: 0.200, 0.125, 0.094, and 0.063, corresponding to a central filter width of 102 × 102, 64 × 64, 48 × 48, and 32 × 32. These phase values were converted to ppm by dividing by $\gamma^* B_0 \text{TE}^* 10^{-6}$ (Petridou et al., 2010).

*Volunteer phase profile comparison*

In each subject, cross sectional profiles were taken through each basal ganglia structure. The percentage decrease in phase from edge-to-middle and edge-to-base was computed and averaged across all subjects, yielding 14 measurements from each structure using Eqs. (1) and (2). This was repeated for each of the four filters. To evaluate if the R2* profile of each structure was indeed flat, the R2* values were measured at the edge and middle of a structure and compared with a paired *t*-test.

*Volunteer phase vs R2* mapping*

Regressions between phase and R2* in different structures were examined with different filter widths and different ROIs. The differences in regression slope between different filter widths are used to examine the effect of filtering on measured phase. For a specific structure, a changing regression slope indicates that structures with higher raw phase are affected more severely by filtering. Correlations between phase and R2* are used to determine the accuracy of phase measures with different filters, ROIs within structures, and baseline ROI measures. Phase and R2* were calculated in basal ganglia structures by averaging voxels within ROIs. ROIs were constructed, based on the R2* map, around whole structures and around selective parts of structures. The same registered ROI was used for R2* and phase measurement. To avoid partial volume effects in the superior–inferior direction, the ROI's were obtained from an R2* image slice where the structure was visible in slices both above and below. The selective ROIs were around the lateral PUT, the medial GP, posterior PUT, posterior lateral PUT, posterior GP, posterior lateral GP and the posterior RN. Selective ROIs were not measured from the SN because of its small shape. The structural phase measures are compared to two baseline phase measures, one from an area of cortical white matter (WM) and another from an area directly adjacent to the structure of interest.

## Results

*Phase behavior in simulation*

Figs. 1 and 2 depict the effects on the susceptibility distribution using the 3D field forward model with various phase filter widths. In both figures, the central phase values within a structure decrease as the filter width increases, with only the extreme edges retaining close to unfiltered values. The susceptibility distribution in Figs. 1a and 2a differs substantially from the unfiltered phase image in Figs. 1b and 2b, which is calculated from the field forward model. In particular, the phase image illustrates field effects from structures outside of the slice due to nonlocal effects of the field distribution. For example, in Fig. 1b phase effects from the RN are evident even though the RN is not within the slice. This out-of-plane field shift can offset the baseline phase of the basal ganglia structures, as demonstrated in the profiles shown in Fig. 3. Because the overall baseline in this region is offset negatively, a decrease in filter size does not necessarily increase the measured phase within a structure (Fig. 3b and d). However, the phase within a structure compared to a baseline immediately outside of the structure is increased.

The unfiltered profiles show that the baseline phase is different from zero because of the nonlocal susceptibility effect of other structures (Fig. 3b and d). This nonzero baseline was manually adjusted by moving the profile along the phase axis until the edges of the raw phase matched the outer edges of the least filtered phase. This allows visual comparison of the difference between the raw profile and the filtered profiles. From Fig. 3b, it appears that phase is most affected by filtering in the middle of the GP because of its large in plane dimension, which leads to a narrower *k*-space representation

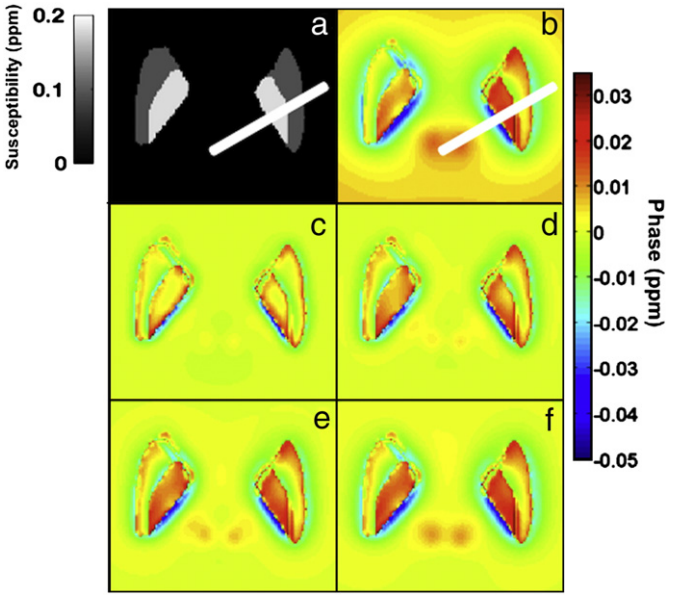


**Fig. 1.** 3D field forward model of the PUT and GP with (a) susceptibility distribution before *k*-space dipole multiplication, (b) unfiltered 3D field forward model, and (c–f) 3D field forward phase model with 4 different filter widths: (c) 0.200, (d) 0.125, (e) 0.094, and (f) 0.063. Units are ppm for phase and ppm for susceptibility. Also cross sectional profiles for Fig. 3 are shown through the GP and PUT in (a) and (b).

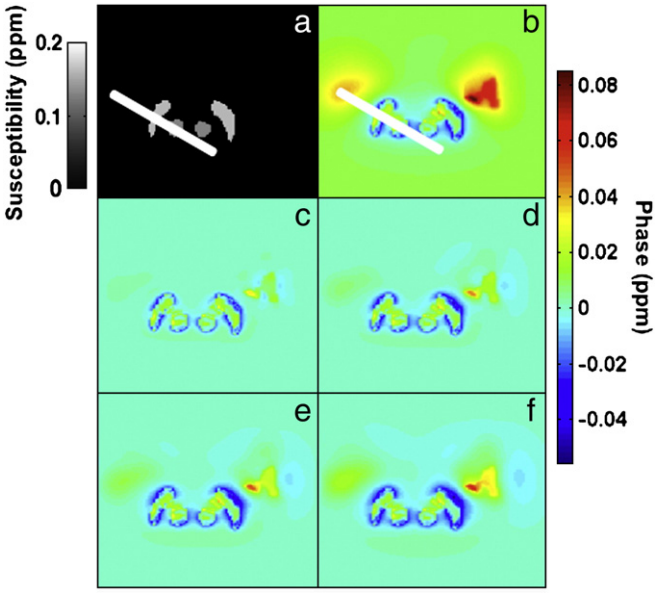


**Fig. 2.** 3D field forward model of the SN and RN with (a) susceptibility distribution before *k*-space dipole multiplication, (b) unfiltered 3D field forward model of the SN and RN, and (c–f) field forward phase model with 4 different filter widths: (c) 0.200, (d) 0.125, (e) 0.094, and (f) 0.063. Units are ppm for field shift and ppm for susceptibility. Also cross sectional profiles for Fig. 3 are shown through the SN and RN in (a) and (b).

that is more strongly affected by the low pass filter. The profile through the PUT seems relatively unaffected by filtering, especially on the lateral border. The profile through the SN and RN shows that the phase within the structure does not vary appreciably with filtering however the phase between the two structures seems to be elevated compared to the susceptibility distribution.

The external field shift effect generated by susceptibility distributions is modeled in Fig. 4, where profiles are shown through the PUT and GP with a susceptibility profile, raw phase profile and filtered phase profile using a 0.125 filter width. Different susceptibility values within the PUT have field shift effects external to its structure and consequently affect the phase profile of the adjacent GP, even though the susceptibility value of the GP remains the same. It appears that the PUT and GP have field effects external to their structure boundaries resulting in phase effects in the neighboring part of the other structure.

The internal field shift effect due to different assigned susceptibilities in the SN shows that the phase values decrease as the susceptibility increases. The assigned susceptibility values of 0.18, 0.16, and 0.14 ppm produced the measured phase values of 0.0107, 0.0133, and 0.0159 ppm (phase) respectively using ROIs around the entire structure. As susceptibility increases in the SN, the phase evolution decreases. This is opposite to what was observed with the increasing susceptibilities in the PUT (Fig. 3). Furthermore, there is an apparent shift in structural borders between the phase and susceptibility profile that is perhaps most pronounced in the SN cross section (Fig. 3c and d) due to the field shift.

### *Volunteer phase profile comparison*

In Fig. 5, in vivo phase and R2* profiles are shown through the GP-PUT and SN-RN for one volunteer. Fortuitously, the raw phase profile shown for the GP-PUT is in line with the global susceptibility change created by the nasal cavity and sinuses, enabling visualization of the unfiltered phase without significant contamination. The profile of the PUT R2* map has a relatively flat shape while the phase does not, because of susceptibility effects from the GP. The raw phase of the PUT is not flat in the profile of the GP and PUT in Fig. 5b, and worsens with increasing filtering, similar to the raw phase of the simulation in Fig. 3b. Tables 1 and 2 compare phase values from in vivo measurements and the simulation using a range of filtering widths. Two measurement locations are used: the difference between edge and central phase value within a structure between filters (Table 1, Eq. (1)), and the difference between the edge and base between filters (Table 2, Eq. (2)). In Table 1, the edge-to-middle phase values show that with increasing filter strength, the phase in the middle of a structure decreases in all structures. The predicted decrease in phase from the edge of a structure to the middle has a similar trend in simulation and experiment for the GP and PUT, but not for the SN and RN. Interestingly, the phase in the PUT is less affected by filtering until the filter width is decreased to 0.063 because the inclined raw phase profile of the PUT has higher spatially varying frequencies than a flat shape. In Table 2, the predicted decrease in phase at the edge of a structure follows the same trend as seen in vivo for all the structures. As the filter width decreases, the phase at the edge of the structure compared to outside of the structure increases.

In contrast to phase, R2* values across each structure showed much less variability. The paired *t*-test for R2* values corresponding to the spatial location of phase measures indicated that the R2* values are the same at the edge and middle of structures in the PUT, SN, and RN, while the R2* is significantly higher ($p<0.05$) in the middle of the GP compared to the edge.

### *Volunteer phase vs R2* mapping*

The location of the phase and R2* measures obtained for regression analysis with PUT, GP, SN, and RN, are shown in Fig. 6 while the scatter plots of R2* vs phase measures are presented in Figs. 7 and 8. The equations for the linear regression lines, correlation coefficients, and *p* values of the slope are found in Tables 3–5. The phase values are highly variable depending upon filter and structure, as discussed below.

In the PUT, the correlation between phase and R2* is generally high and is improved with ROI placement and filter width adjustment. The ROI structural measurements reveal that whole structure measurements

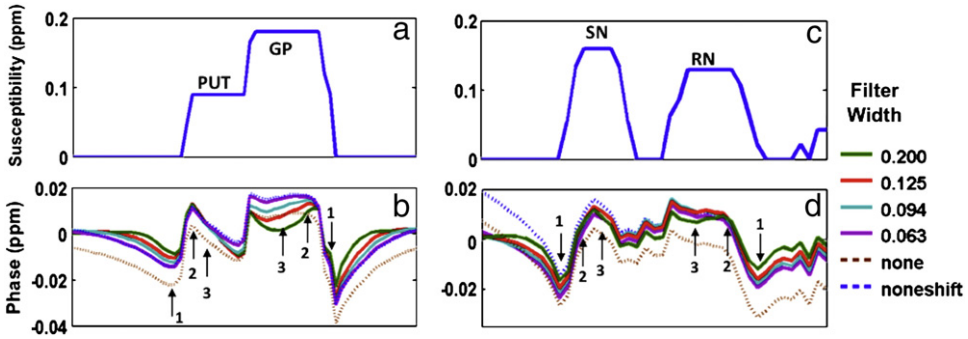


**Fig. 3.** Susceptibility and phase profiles of the GP, PUT, SN, and RN from the cross sections shown in Figs. 1 and 2. Cross sectional susceptibility profile (in ppm) of (a) GP and PUT and (c) SN and RN. Phase profile of (b) GP and PUT and (d) SN and RN. Phase profiles used 4 different filter widths in solid lines (0.200, 0.125, 0.094, and 0.063), and show the raw phase profile and the phase axis shifted phase profile (dotted lines). The raw phase is aligned along the phase axis so the structure borders have the same phase value. Arrows in (b) and (d) show the measurement locations for Eqs. (1) and (2), with arrow 1: base, arrow 2: edge, and arrow 3: middle.

show a weaker correlation ($R=0.71$) compared to measuring the posterior part of the structure ($R=0.90$) with the smallest filter width of 0.063. Also of note, the slope of the regression line is less variable when the phase is measured at the lateral border ($4.20–4.55\times10^{-4}$ ppm*s) of the structure compared to around its entirety ($3.12–5.10\times10^{-4}$ ppm*s) (Fig. 7a–d and Table 3). As well, the correlation between phase and R2* is similar when baseline phase measures are obtained from a nearby section of cortical WM or when taken immediately outside of the structure.

In the GP, although the size, shape, and orientation is similar to that of the PUT, the regression analysis between phase and R2* are markedly different. The regression between phase and R2* in the GP across subjects is only significant when measured at the edge of the structure and even then only has a moderate correlation of $R=0.52$ using a filter width of 0.094 (Fig. 7e, f and Table 4). As opposed to the PUT measurements, the correlation coefficient is not significant when the baseline phase is measured immediately outside of the GP.

The SN regression between phase and R2* is negative (Fig. 8a, b and Table 5), which agrees with the simulated results. The correlation between phase and R2* appears higher when phase is compared to a baseline adjacent to the SN ($R=0.67$) versus the cortical WM baseline ($R=0.54$) using a filter width of 0.125. In the SN, there was visible artifact when the filter width was set to 0.063.

In the RN, as seen with the regression analysis of the SN, there appears to be a higher correlation between phase and R2* in the RN with the baseline phase measure obtained adjacent to the structure ($R=0.81$) compared to cortical WM ($R=0.72$) using a filter width of 0.125 (Figs. 8c-f and Table 5). There is less variation in the slope of the regression when the structural ROI is taken at the posterior aspect of the structure ($4.19–6.85\times10^{-4}$ ppm*s) compared to an ROI around the whole structure ($3.22–6.59\times10^{-4}$ ppm*s), not including the 0.063 filter width because wrapping artifact was apparent within the structure.

## Discussion

The main factors examined in this study that contribute to phase values produced by a susceptibility distribution are structural geometry, filtering, and external field shift effects from other susceptibility sources. Our work has shown that more accurate phase measurements can be obtained with careful attention to where the baseline phase comparison is obtained, what subsections of the structure are measured, and appropriate choice of filter width for the size and location of a structure. While new background phase removal methods and susceptibility mapping techniques are evolving, the simplicity and availability of standard phase imaging explain the current widespread use and support the future consideration of the method in iron accumulation studies.

The susceptibility distribution of a deep grey matter structure can cause field effect changes within and around that structure, potentially having an adverse effect on measured phase. This is demonstrated both in simulation and in vivo phase images. The in vivo cross sectional profile through the GP and PUT shows that the phase profile in the PUT is slanted towards the GP while the R2* profile is flat. As shown in the simulation profiles, the lateral aspect of the PUT, the medial aspect of the GP and the posterior aspect of the RN are less affected by surrounding susceptibility distributions in both unfiltered and filtered phase images. Therefore, phase should not be measured from areas that are highly influenced by external field effects such as the medial PUT or the lateral GP.

While a susceptibility distribution can cause external field shift effects, the internal phase depends not only on the susceptibility, but also on the shape of the structure. The in vivo profile (Fig. 3) and axial phase image (Figs. 1 and 2) demonstrate that the phase within a structure depends on the shape, which is perhaps most pronounced in the SN. In the simulation and in vivo profile, the lateral borders of the SN show less phase evolution making it difficult to discern the

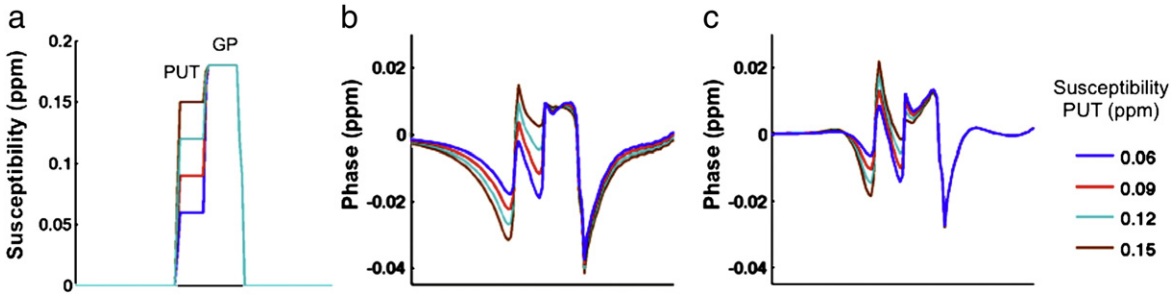


**Fig. 4.** Cross sectional field shift values of the GP and PUT with different susceptibility values assigned to the PUT. (a) Susceptibility distribution (b) raw field map (c) filtered field map. Filter width 0.125.

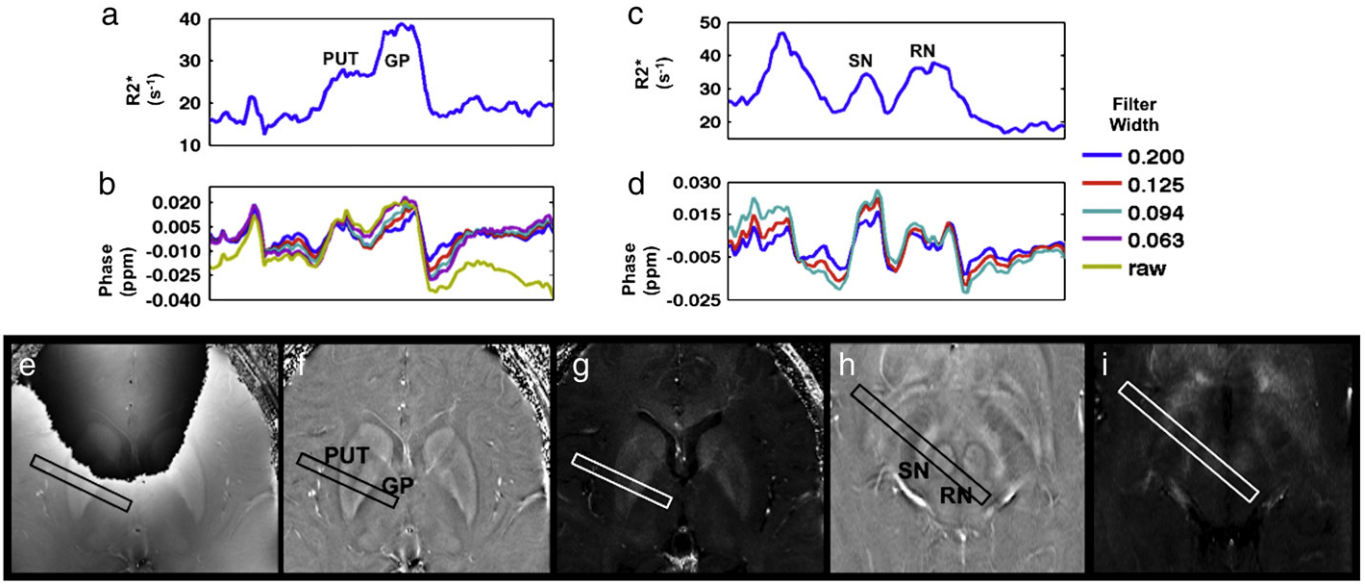


**Fig. 5.** In vivo cross sectional profiles of (a) R2* and (b) phase with different size filter widths across the PUT and GP. The raw phase in (b) is adjusted along the phase axis to align the phase of the outside of both structures since the raw phase is arbitrary. Cross sectional profiles of (c) R2* and (d) phase with different filter widths across the SN and RN. Axial images of (e) raw phase and (f) filtered phase, with a filter width of 0.125 for the GP and PUT, TE = 16 ms. (g) Axial R2* map of the GP and PUT. (h) Filtered phase with a filter width of 0.125 showing the SN and RN, TE = 16 ms. (i) R2* map of the SN and RN. The rectangular section has a width of 12 pixels in e-g and 8 pixels in h-i. The pixels along the width of the rectangular section are averaged to produce the graphs in a–d to mitigate the effects of noisy pixels and create a smoother profile for more accurate phase measurements.

structure's true edge. This effect makes it appear as though the edge is shifted in the phase image compared to the R2* map, which has been described for other structures in phase imaging (O'Gorman et al., 2010). Since the edge shift appears in both in vivo and simulated, non-filtered phase images, it seems that the apparent edge shift is due to structural geometry combined with the dipole field effect (Deistung et al., 2008). Therefore ROIs should be drawn around the magnitude image (or R2* image) and not the phase image, if phase within the true structure is to be measured.

When comparing phase measures within structures to known brain iron concentrations, phase may not be reliable between different structures, as seen by the wide variability in regression slopes between phase and R2* between structures, but could be used to evaluate the relative iron changes in the same structure across subjects. Several studies have compared phase across different structures to estimated iron content (Hopp et al., 2010; Wharton and Bowtell, 2010), however a more appropriate measure would be phase within one structure across subjects (Hammond et al., 2008b; Pfefferbaum et al., 2009). The variability in the regression between phase and R2* between structures is exemplified by the negative regression in the SN which is attributed to the complicated three-dimensional geometry of the structure, unlike the more cylindrical RN. This could be an important feature when studying the SN because it has been reported that the phase evolves with Parkinson's disease progression and iron accumulation (Zhang et al., 2010), or in normal individuals with ageing (Haacke et al., 2010; Xu et al., 2008). However our study shows phase evolution in the opposite direction with increasing iron content, although all results are significant. Due to the nonlocal dipolar effects as seen in Figs. 1 and 2, the most intense phase may be outside of the structure in the superior–inferior plane. With ROI placement based on phase imaging only, the measured phase could be outside of the actual structure, in the superior imaging slice. As well, the in-plane edges of the structure may be difficult to discern due to phase geometry effects as seen in Fig. 3. The ROIs in our study were drawn on R2* images to eliminate the out-of-plane phase effects and the ambiguity at the edges of structures on the phase images. While the out-of-plane measure on phase images could prove useful, it is important to accurately describe the spatial location of ROIs in

**Table 1**
Fractional phase difference of deep grey structures from edge to middle compared to adjacent baseline—in vivo and simulation.

| Structure | Filter width | In vivo phase edge to middle (ppm ± stdev) | Simulated phase edge to middle (ppm) |
|---|---|---|---|
| PUT | 0.2 | 0.22 ± 0.06 | 0.30 |
| | 0.125 | 0.19 ± 0.09 | 0.32 |
| | 0.094 | 0.19 ± 0.10 | 0.28 |
| | 0.063 | 0.13 ± 0.10 | 0.24 |
| GP | 0.2 | 0.20 ± 0.08 | 0.23 |
| | 0.125 | 0.10 ± 0.08 | 0.11 |
| | 0.094 | −0.01 ± 0.12 | 0.04 |
| | 0.063 | −0.08 ± 0.16 | −0.03 |
| SN | 0.2 | −0.05 ± 0.14 | −0.06 |
| | 0.125 | −0.17 ± 0.18 | −0.11 |
| | 0.094 | −0.25 ± 0.20 | −0.14 |
| RN | 0.2 | 0.18 ± 0.14 | −0.01 |
| | 0.125 | 0.06 ± 0.14 | −0.05 |
| | 0.094 | −0.03 ± 0.16 | −0.08 |

**Table 2**
Fractional phase difference of deep grey structure edges — in vivo and simulation.

| Structure | Filter width | In vivo phase edge difference compared to smallest filter (ppm ± stdev) | Simulated phase edge differences (ppm) |
|---|---|---|---|
| PUT | 0.2 | −0.35 ± 0.06 | −0.29 |
| | 0.125 | −0.15 ± 0.04 | −0.13 |
| | 0.094 | −0.07 ± 0.03 | −0.10 |
| | 0.063 | 0.00 ± 0.00 | 0.00 |
| GP | 0.2 | −0.44 ± 0.13 | −0.30 |
| | 0.125 | −0.19 ± 0.09 | −0.13 |
| | 0.094 | −0.05 ± 0.08 | −0.06 |
| | 0.063 | 0.00 ± 0.00 | 0.00 |
| SN | 0.2 | −0.42 ± 0.10 | −0.15 |
| | 0.125 | −0.15 ± 0.04 | −0.04 |
| | 0.094 | 0.00 ± 0.00 | 0.00 |
| RN | 0.2 | −0.31 ± 0.12 | −0.24 |
| | 0.125 | −0.08 ± 0.05 | −0.04 |
| | 0.094 | 0.00 ± 0.00 | 0.00 |

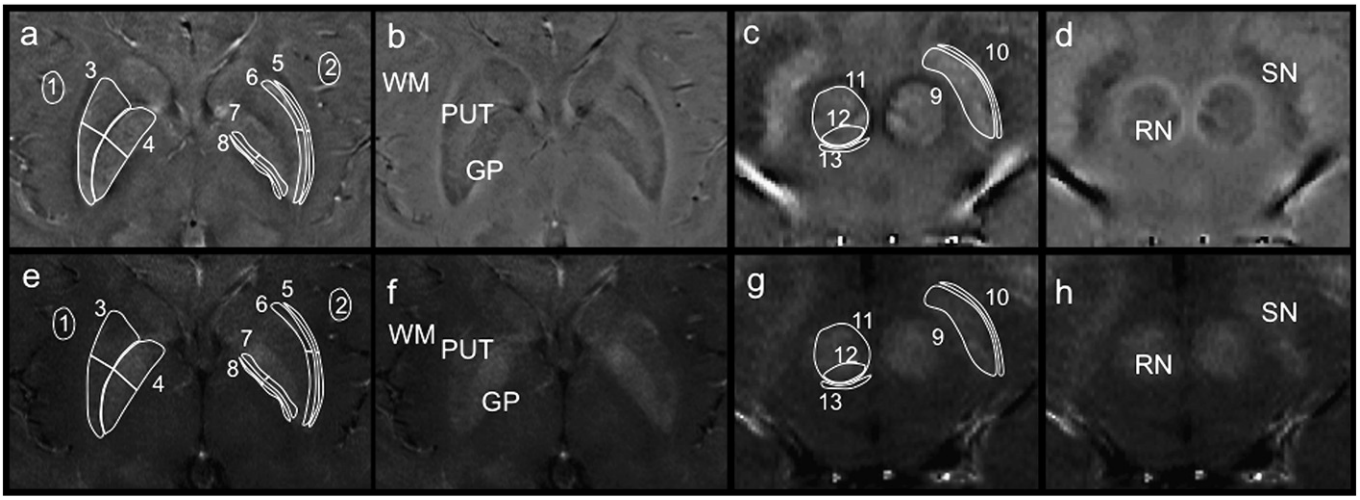


**Fig. 6.** Phase images (top row) and R2* images (bottom row) illustrating ROI placement. The top row illustrates inverted phase images (a and c) as used for comparison to R2* values, and traditional phase images of the same slice (b and d), with stronger susceptibility sources having a more negative value. The bottom row of R2* images show larger R2* values as being brighter. The ROI's are identified by numbers on the two slice locations (a, b, d, f) GP, PUT and (c, d, g, h) RN, SN. (1) and (2) are sections of cortical WM. (3) the entire PUT and posterior PUT, (4) the entire GP and posterior GP, (5) the lateral and lateral posterior baseline adjacent to the PUT, (6) the lateral and lateral posterior aspect of PUT, (7) the medial and medial posterior aspect of GP, (8) the medial and medial posterior baseline adjacent to the GP, (9) the entire SN, (10) the adjacent baseline of SN, (11) the entire RN, (12) the posterior aspect of RN, and (13) the adjacent baseline of the RN. Sections of cortex white matter are not shown for the RN SN but are in similar position to (1) and (2) but in the axial slice of the RN SN.

both phase and magnitude images for reproducibility and comparison with other studies.

The baseline phase in an image is somewhat arbitrary and depends on factors such as shimming and global susceptibility effects therefore phase measured in structures is typically compared to another region in the brain. As well, neighboring susceptibility sources outside of the slice of interest must also be considered in order to obtain an accurate phase measure, as demonstrated in the simulation of the SN and RN. When using axial plane slices, it is somewhat fortuitous that the inferior SN and RN are not directly in line with the more superior GP and PUT, which means these iron-rich structures do not have a direct effect on each other, but do have an effect on the neighboring background. To overcome this, the baseline phase measurement should be obtained directly adjacent to the structure of interest to mitigate the effects of other susceptibility sources such as air tissue interfaces or endogenous structures. The in vivo data shows higher correlations between phase and R2* when baseline measures of phase are obtained adjacent to structures compared to a distant area of cortical WM in the SN and RN. The GP correlation was not stronger with the adjacent baseline measure possibly because of the close proximity of the SN causing a strong susceptibility effect. The correlations between phase and R2* were similar for the PUT with both baseline measures, possibly because both measures are close in proximity.

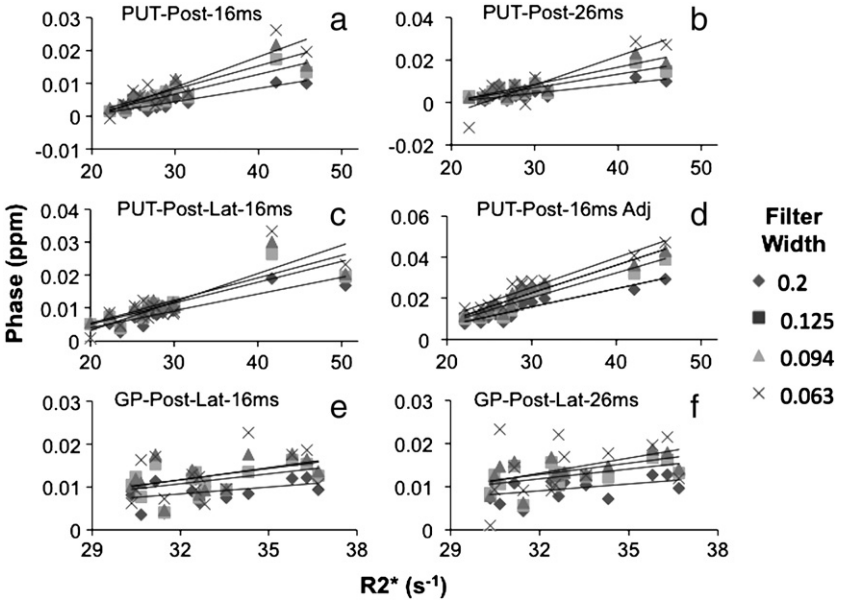


**Fig. 7.** Phase vs R2* linear regression of the GP and PUT from 7 healthy volunteers, with each scatter plot showing 4 different filters: 0.200, 0.125, 0.094, and 0.063. (a, b) Posterior half of the PUT (a) 16 ms TE (b) 26 ms TE, (c) posterior lateral aspect of the PUT 16 ms TE. Field shift measures in a–c are compared to a section of cortical WM (Fig. 6). (d) Posterior aspect of the PUT compared to measure adjacent to PUT 16 ms TE. (e, f) Posterior lateral aspect of the GP compared to a section of cortical WM with (e) 16 ms TE, and (f) 26 ms TE.

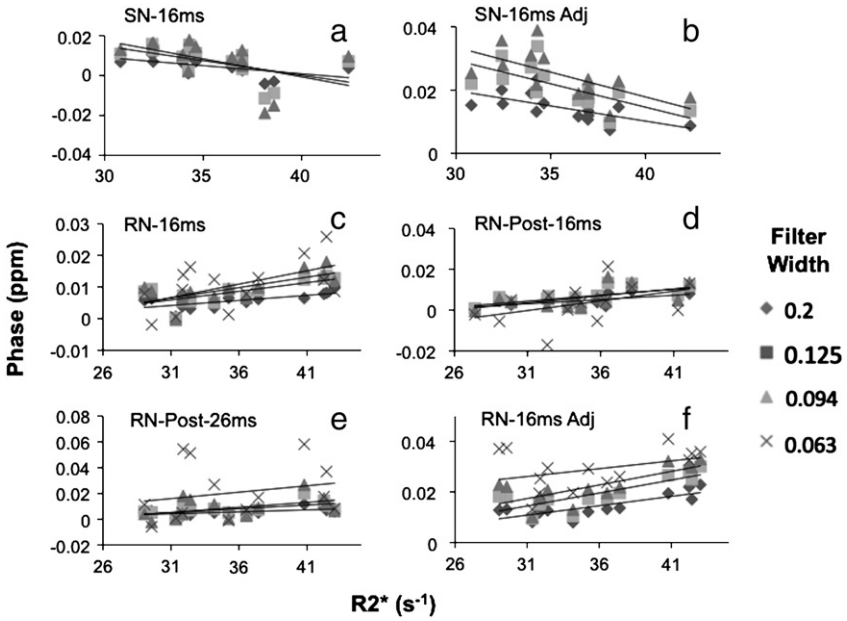


**Fig. 8.** Phase vs R2* regression of the SN and RN. (a, b) Whole SN 16 ms TE with phase compared to section of cortical WM in (a) and adjacent to SN in (b). (c) Whole RN 16 ms TE (d) posterior aspect of RN 16 ms TE, (e) whole RN 26 ms TE. Measured phase in c–e is compared to a section of cortical WM (Fig. 6). (f) Whole RN 16 ms TE compared to phase directly posterior to structure. Each scatter plot shows 4 different filters: 0.200, 0.125, 0.094, and 0.063.

Measuring the edge phase rather than the whole structure gives less change in slope of the regression line for PUT, GP, and RN. As well, when the whole structure was measured, the slope of the regression decreased as the filter strength increased. This supports the idea that filtering affects the measured phase more in structures with a higher iron content within axially viewed structures compared to the same structures with lower iron content. As well, the filtering effect is stronger in the center of structures. This filtering effect is most clearly demonstrated in the GP as the correlation between phase and R2* is weak and is only significant when the ROI is measured around the medial border. The large in-plane dimensions of the GP and its high iron content leads to lower phase values post filtering in the middle of the structure. Haacke et al. (2007) found that measuring phase from different ROIs in the PUT produced drastically different phase results and attributed this to different iron accumulation patterns. As well, Zivadinov et al. (2010) and Haacke et al. (2010) described iron accumulation patterns in the GP and PUT and Grabner et al. (2010) describe iron accumulation in the posterior aspect of the PUT in Parkinson's disease. These patterns are similar to the results of filtering and dipole effects demonstrated in Figs. 1 and 2. This suggests that the observed iron accumulation pattern in these studies with the standard phase filtering method might be attributed to filtering and susceptibility dipole effects. With the standard phase filtering method, an increase in iron may not show a large increase in phase within a highly filtered area. To overcome this, ROIs should be placed around specific parts of structures and these sub-ROIs analyzed across subjects to better reveal the pattern of iron changes. Therefore, iron accumulation patterns within specific structures could be studied

**Table 3**
Phase - R2* regression for PUT with TE-phase = 16 ms.

| Phase measure (baseline) | Filter width | Slope (ppm*s) $\times 10^{-4}$ | $R$ | $p$-Value |
|---|---|---|---|---|
| Whole (baseline cortical) | 0.2 | 3.12 | 0.87 | 0.00 |
| | 0.125 | 4.28 | 0.88 | 0.00 |
| | 0.094 | 4.67 | 0.84 | 0.00 |
| | 0.063 | 5.10 | 0.71 | 0.00 |
| Whole (baseline adjacent) | 0.2 | 7.63 | 0.82 | 0.00 |
| | 0.125 | 10.07 | 0.83 | 0.00 |
| | 0.094 | 11.17 | 0.84 | 0.00 |
| | 0.063 | 11.13 | 0.82 | 0.00 |
| Lateral (baseline cortical) | 0.2 | 4.20 | 0.86 | 0.00 |
| | 0.125 | 4.55 | 0.77 | 0.00 |
| | 0.094 | 4.25 | 0.68 | 0.01 |
| | 0.063 | 4.21 | 0.60 | 0.02 |
| Posterior (baseline cortical) | 0.2 | 4.07 | 0.93 | 0.00 |
| | 0.125 | 6.01 | 0.92 | 0.00 |
| | 0.094 | 7.09 | 0.90 | 0.00 |
| | 0.063 | 9.26 | 0.90 | 0.00 |
| Posterior lateral (baseline cortical) | 0.2 | 5.08 | 0.90 | 0.00 |
| | 0.125 | 6.35 | 0.87 | 0.00 |
| | 0.094 | 6.83 | 0.84 | 0.00 |
| | 0.063 | 8.59 | 0.84 | 0.00 |
| Posterior (baseline adjacent) | 0.2 | 8.87 | 0.93 | 0.00 |
| | 0.125 | 12.05 | 0.95 | 0.00 |
| | 0.094 | 13.54 | 0.95 | 0.00 |
| | 0.063 | 14.38 | 0.95 | 0.00 |

**Table 4**
Phase - R2* regression for GP with TE-phase = 16 ms.

| Phase measure (baseline) | Filter width | Slope (ppm*s) $\times 10^{-4}$ | $R$ | $p$-Value |
|---|---|---|---|---|
| Whole (baseline cortical) | 0.2 | 1.10 | 0.16 | 0.59 |
| | 0.125 | 0.81 | 0.08 | 0.79 |
| | 0.094 | 0.12 | 0.01 | 0.98 |
| | 0.063 | 2.84 | 0.12 | 0.68 |
| Lateral (baseline cortical) | 0.2 | 4.16 | 0.40 | 0.15 |
| | 0.125 | 6.06 | 0.50 | 0.07 |
| | 0.094 | 7.72 | 0.52 | 0.05 |
| | 0.063 | 10.99 | 0.44 | 0.12 |
| Posterior (baseline cortical) | 0.2 | −0.59 | 0.06 | 0.83 |
| | 0.125 | −1.14 | 0.09 | 0.77 |
| | 0.094 | −0.99 | 0.06 | 0.83 |
| | 0.063 | 2.56 | 0.11 | 0.70 |
| Posterior lateral (baseline cortical) | 0.2 | 5.35 | 0.41 | 0.15 |
| | 0.125 | 7.73 | 0.48 | 0.08 |
| | 0.094 | 8.74 | 0.47 | 0.09 |
| | 0.063 | 9.52 | 0.40 | 0.16 |
| Posterior lateral (baseline adjacent) | 0.2 | 9.66 | 0.32 | 0.27 |
| | 0.125 | 12.54 | 0.34 | 0.23 |
| | 0.094 | 14.63 | 0.39 | 0.17 |
| | 0.063 | 16.09 | 0.41 | 0.15 |

**Table 5**
Phase-R2* regression for RN and SN with TE-phase = 16 ms.

| Phase measure (baseline) | Filter width | Slope (ppm*s) $\times 10^{-4}$ | $R$ | $p$-Value |
|---|---|---|---|---|
| RN whole (baseline cortical) | 0.2 | 3.22 | 0.69 | 0.01 |
| | 0.125 | 5.48 | 0.72 | 0.00 |
| | 0.094 | 6.59 | 0.71 | 0.00 |
| | 0.063 | 8.47 | 0.55 | 0.04 |
| RN whole (baseline adjacent) | 0.2 | 7.41 | 0.80 | 0.00 |
| | 0.125 | 10.24 | 0.81 | 0.00 |
| | 0.094 | 10.73 | 0.76 | 0.00 |
| | 0.063 | 6.17 | 0.37 | 0.19 |
| RN posterior (baseline cortical) | 0.2 | 4.19 | 0.64 | 0.01 |
| | 0.125 | 5.83 | 0.62 | 0.02 |
| | 0.094 | 6.85 | 0.58 | 0.03 |
| | 0.063 | 9.47 | 0.43 | 0.13 |
| SN whole (baseline cortical) | 0.2 | −8.24 | 0.58 | 0.03 |
| | 0.125 | −14.64 | 0.54 | 0.04 |
| | 0.094 | −18.14 | 0.49 | 0.08 |
| | 0.063 | −18.59 | 0.33 | 0.25 |
| SN whole (baseline adjacent) | 0.2 | −9.58 | 0.65 | 0.01 |
| | 0.125 | −14.74 | 0.67 | 0.01 |
| | 0.094 | −15.66 | 0.64 | 0.01 |
| | 0.063 | −13.96 | 0.51 | 0.06 |

with the standard phase filtering method if many subROIs are examined.

Filter width should be chosen based on structure shape, size, and regional susceptibility influences. The simulation would suggest that the lowest filter width is the most desirable to remove the slow varying phase effects, as the phase values in a structure are least affected both in the middle and at the edges of the structures. However, the in vivo data suggest susceptibility artifact from the sinuses and other baseline phase influences, while not visually apparent, can alter the inherent phase measures due to local susceptibility, therefore the smallest filter width is not always appropriate. This is apparent with the relatively lower correlation between phase and R2* in the RN and SN with the smallest filter width compared to phase measures with higher filter widths in these structures. As well, measuring phase in the PUT benefits with a higher R2* vs phase correlation when ROIs are taken in the posterior aspect of the structure, compared to the whole structure. This effect in the SN, RN, and anterior PUT at small filter widths is due to the background susceptibility effect from the air tissue interface of the paranasal sinuses and nasal cavity. The slope of the regression between phase and R2* in a structure increases as filter width decreases which is desired in neurological studies to separate high from low iron containing structures. However, as the filter width decreases, the correlation between phase and R2* decreases, which reduces the power of statistical analysis in discerning normal from high iron accumulation states. This correlation is increased by measuring the baseline ROI directly adjacent to the structure of interest to mitigate the effects of background susceptibility.

Because the SN and RN are smaller structures with broader $k$-space representations, it is expected that there would not be as much phase variation measured in simulation with Eq. (1) across different filter widths. However the in vivo results show that there is considerable variation with filter width. A drawback of the simulation is the assumption of homogenous susceptibility throughout each structure and no susceptibility effect from other brain tissue. While the paired $t$-test for R2* measures from edge to middle of a structure show homogeneity of R2* measures for the PUT, SN and RN, this is for only one axial slice and for one cross section. A zero susceptibility value was assigned to surrounding tissue to clarify iron rich structure effects and because the distant baseline phase is not used in any simulation measurements. The influence of other external tissues is not accounted for in the model and this could produce additional susceptibility effects giving rise to the differences found in vivo. Nevertheless, the simplistic model served to clarify and accurately predict effects in the GP and PUT.

Some studies have investigated susceptibility mapping techniques (de Rochefort et al., 2010; Shmueli et al., 2009; Wharton et al., 2010), an image processing step after phase imaging, which removes dipolar artifacts from phase images to find susceptibility distributions. While these techniques look promising to uncover accurate brain susceptibility values, they are currently complicated to implement with issues such as highly involved image processing, multiple patient orientations, or image artifact.

To optimize the precision of phase imaging for estimating tissue susceptibility, ROIs should be placed and interpreted with knowledge of external phase effects and filtering effects, and baseline phase measures should be obtained immediately adjacent to the SN and RN and close to the PUT for the PUT and GP measures. Many sub-ROIs should be obtained across subjects, in order to discern the relative quantity and location of iron accumulation within a structure. Although phase is influenced by filtering and external susceptibility sources, good correlations are observed between phase measures and R2*. Smaller filter widths will elucidate the differences between high iron and low iron states while adjacent baseline phase measures will improve the accuracy of the measured phase. Of the filter widths used in this study, the best choices are 0.125 for the SN and RN and 0.094 for the GP and PUT or 0.063 for the posterior GP and PUT to remove the global susceptibility effect and preserve the phase due to endogenous brain structures.

## Conclusions

Phase imaging with the high pass filtering method uses standard MRI sequences and processing software that are widely available, and reveals susceptibility information that was previously confounded by other tissue parameters. The accuracy of measured phase to tissue susceptibility was optimized using simulated phase images, to predict both field effects and filtering effects, and was verified in vivo by comparing phase to R2*. The simulated field effects, as demonstrated in sectional profiles, showed the most profound effects in the PUT from the external field effects caused by the neighboring GP and substantial changes in baseline phase around the SN and RN. The in vivo phase comparison to R2* showed that phase is most accurately measured on a structure by structure basis, with appropriate filter width for the size of structure, and with the background phase obtained directly adjacent to the SN and RN. Using a standard filter of 0.125 the slopes and correlation coefficients were $4.28\times10^{-4}$ ppm*s and $R=0.88$ for the PUT, $0.81\times10^{-4}$ppm*s and $R=0.08$ for the GP, $5.48\times10^{-4}$ ppm*s and $R=0.72$ for the RN and $-14.64\times10^{-4}$ ppm*s and $R=0.54$ for the SN. To achieve the most effective correlation to R2* we recommend using a filter width of 0.094 for the GP and PUT and 0.125 for the SN and RN. The baseline phase measure should be obtained directly adjacent to the SN, and RN as opposed to an area of distant cortical WM. The correlation improved using the adjacent measures compared to the cortical measure in the SN from $R=0.54$ to 0.67 and in the RN from $R=0.72$ to 0.81, using a filter width of 0.125. Different regression slopes are seen between subROIs within structures suggesting that regional iron accumulation within a structure is best studied with subROIs between different subject groups, not differences in phase values relative to the overall phase in one structure. Phase imaging has the potential for more sensitive comparisons of brain iron accumulation in deep grey matter if specific filtering parameters and susceptibility effects are carefully considered.

## Acknowledgments

Operating grants from the Canadian Institutes of Health Research (CIHR) and the Natural Sciences and Engineering Research Council of Canada (NSERC) are acknowledged. AJW was supported by a Vanier

Canada Graduate Scholarship, and an Alberta Innovates Health Solutions MD/PhD studentship.

## References


Bartzokis, G., Tishler, T.A., 2000. MRI evaluation of basal ganglia ferritin iron and neurotoxicity in Alzheimer's and Huntingon's disease. Cell. Mol. Biol. 46, 821–833.

Baudrexel, S., Nurnberger, L., Rub, U., Seifried, C., Klein, J.C., Deller, T., Steinmetz, H., Deichmann, R., Hilker, R., 2010. Quantitative mapping of T1 and T2* discloses nigral and brainstem pathology in early Parkinson's disease. Neuroimage 51, 512–520.

Bermel, R.A., Puli, S.R., Rudick, R.A., Weinstock-Guttman, B., Fisher, E., Munschauer III, F. E., Bakshi, R., 2005. Prediction of longitudinal brain atrophy in multiple sclerosis by gray matter magnetic resonance imaging T2 hypointensity. Arch. Neurol. 62, 1371–1376.

Deistung, A., Rauscher, A., Sedlacik, J., Stadler, J., Witoszynskyj, S., Reichenbach, J.R., 2008. Susceptibility weighted imaging at ultra high magnetic field strengths: theoretical considerations and experimental results. Magn. Reson. Med. 60, 1155–1168.

Denk, C., Rauscher, A., 2010. Susceptibility weighted imaging with multiple echoes. J. Magn. Reson. Imaging 31, 185–191.

de Rochefort, L., Liu, T., Kressler, B., Liu, J., Spincemaille, P., Lebon, V., Wu, J.L., Wang, Y., 2010. Quantitative susceptibility map reconstruction from MR Phase data using Bayesian regularization: validation and application to brain imaging. Magn. Reson. Med. 63, 194–206.

Du, Y.P.P., Jin, Z.Y., Hu, Y.Z., Tanabe, J., 2009. Multi-echo acquisition of MR angiography and venography of the brain at 3 Tesla. J. Magn. Reson. Imaging 30, 449–454.

Duyn, J.H., van Gelderen, P., Li, T.Q., de Zwart, J.A., Koretsky, A.P., Fukunaga, M., 2007. High-field MRI of brain cortical substructure based on signal phase. Proc. Natl. Acad. Sci. U. S. A. 104, 11796–11801.

Eissa, A., Lebel, R.M., Korzan, J.R., Zavodni, A.E., Warren, K.G., Catz, I., Emery, D.J., Wilman, A.H., 2009. Detecting lesions in multiple sclerosis at 4.7 Tesla using phase susceptibility-weighting and T2-weighting. J. Magn. Reson. Imaging 30, 737–742.

Grabner, G., Haubenberger, D., Rath, J., Beisteiner, R., Auff, E., Trattnig, S., Barth, M., 2010. A population-specific symmetric phase model to automatically analyze susceptibility-weighted imaging (SWI) phase shifts and phase symmetry in the human brain. J. Magn. Reson. Imaging 31, 215–220.

Gupta, D., Saini, J., Kesavadas, C., Sarma, P.S., Kishore, A., 2010. Utility of susceptibility-weighted MRI in differentiating Parkinson's disease and atypical parkinsonism. Neuroradiology 52, 1087–1094.

Haacke, E.M., Xu, Y., Cheng, Y.C., Reichenbach, J.R., 2004. Susceptibility weighted imaging (SWI). Magn. Reson. Med. 52, 612–618.

Haacke, E.M., Ayaz, M., Khan, A., Manova, E.S., Krishnamurthy, B., Gollapalli, L., Ciulla, C., Kim, I., Petersen, F., Kirsch, W., 2007. Establishing a baseline phase behavior in magnetic resonance imaging to determine normal vs. abnormal iron content in the brain. J. Magn. Reson. Imaging 26, 256–264.

Haacke, E.M., Makki, M., Ge, Y.L., Maheshwari, M., Sehgal, V., Hu, J.N., Selvan, M., Wu, Z., Latif, Z., Xuan, Y., Khan, O., Garbern, J., Grossman, R.I., 2009a. Characterizing iron deposition in multiple sclerosis lesions using susceptibility weighted imaging. J. Magn. Reson. Imaging 29, 537–544.

Haacke, E.M., Mittal, S., Wu, Z., Neelavalli, J., Cheng, Y.C., 2009b. Susceptibility-weighted imaging: technical aspects and clinical applications, part 1. AJNR. Am. J. Neuroradiol. 30, 19–30.

Haacke, E.M., Miao, Y., Liu, M., Habib, C.A., Katkuri, Y., Liu, T., Yang, Z., Lang, Z., Hu, J., Wu, J., 2010. Correlation of putative iron content as represented by changes in R2* and phase with age in deep gray matter of healthy adults. J. Magn. Reson. Imaging 32, 561–576.

Hammond, K.E., Lupo, J.M., Xu, D., Metcalf, M., Kelley, D.A., Pelletier, D., Chang, S.M., Mukherjee, P., Vigneron, D.B., Nelson, S.J., 2008a. Development of a robust method for generating 7.0 T multichannel phase images of the brain with application to normal volunteers and patients with neurological diseases. Neuroimage 39, 1682–1692.

Hammond, K.E., Metcalf, M., Carvajal, L., Okuda, D.T., Srinivasan, R., Vigneron, D., Nelson, S.J., Pelletier, D., 2008b. Quantitative in vivo magnetic resonance imaging of multiple sclerosis at 7 Tesla with sensitivity to iron. Ann. Neurol. 64, 707–713.

He, X., Yablonskiy, D.A., 2009. Biophysical mechanisms of phase contrast in gradient echo MRI. Proc. Natl. Acad. Sci. U. S. A. 106, 13558–13563.

Hopp, K., Popescu, B.F., McCrea, R.P., Harder, S.L., Robinson, C.A., Haacke, M.E., Rajput, A. H., Rajput, A., Nichol, H., 2010. Brain iron detected by SWI high pass filtered phase calibrated with synchrotron X-ray fluorescence. J. Magn. Reson. Imaging 31, 1346–1354.

Langkammer, C., Krebs, N., Goessler, W., Scheurer, E., Ebner, F., Yen, K., Fazekas, F., Ropele, S., 2010. Quantitative MR imaging of brain iron: a postmortem validation study. Radiology 257, 455–462.

Lee, J., Hirano, Y., Fukunaga, M., Silva, A.C., Duyn, J.H., 2010a. On the contribution of deoxy-hemoglobin to MRI gray-white matter phase contrast at high field. Neuroimage 49, 193–198.

Lee, J., Shmueli, K., Fukunaga, M., van Gelderen, P., Merkle, H., Silva, A.C., Duyn, J.H., 2010b. Sensitivity of MRI resonance frequency to the orientation of brain tissue microstructure (vol 107, pg 5130, 2010). Proc. Natl. Acad. Sci. U. S. A. 107, 5130–5135.

Marques, J.P., Bowtell, R., 2005. Application of a Fourier-based method for rapid calculation of field inhomogeneity due to spatial variation of magnetic susceptibility. Concepts Magn. Reson. Part B Mag. Reson. Eng. 25B (1), 65–78.

Mitsumori, F., Watanabe, H., Takaya, N., 2009. Estimation of brain iron concentration in vivo using a linear relationship between regional iron and apparent transverse relaxation rate of the tissue water at 4.7 T. Magn. Reson. Med. 62, 1326–1330.

Neelavalli, J., Cheng, Y.C.N., Jiang, J., Haacke, E.M., 2009. Removing background phase variations in susceptibility-weighted imaging using a fast, forward-field calculation. J. Magn. Reson. Imaging 29, 937–948.

Ogg, R.J., Langston, J.W., Haacke, E.M., Steen, R.G., Taylor, J.S., 1999. The correlation between phase shifts in gradient-echo MR images and regional brain iron concentration. Magn. Reson. Imaging 17, 1141–1148.

O'Gorman, R.L., Shmueli, K., Ashkan, K., Samuel, M., Lythgoe, D.J., Shahidiani, A., Wastling, S.J., Footman, M., Selway, R.P., Jarosz, J., 2010. Optimal MRI methods for direct stereotactic targeting of the subthalamic nucleus and globus pallidus. Eur. Radiol. 21 (1), 130–136.

Petridou, N., Wharton, S.J., Lotfipour, A., Gowland, P., Bowtell, R., 2010. Investigating the effect of blood susceptibility on phase contrast in the human brain. Neuroimage 50, 491–498.

Pfefferbaum, A., Adalsteinsson, E., Rohlfing, T., Sullivan, E.V., 2009. MRI estimates of brain iron concentration in normal aging: comparison of field-dependent (FDRI) and phase (SWI) methods. Neuroimage 47, 493–500.

Pinero, D.J., Connor, J.R., 2000. Iron in the brain: an important contributor in normal and diseased states. Neuroscientist 6, 435–453.

Rossi, M., Ruottinen, H., Elovaara, I., Ryymin, P., Soimakallio, S., Eskola, H., Dastidar, P., 2010. Brain iron deposition and sequence characteristics in parkinsonism: comparison of SWI, T2* maps, T2-weighted-, and FLAIR-SPACE. Invest. Radiol. 45, 795–802.

Salomir, R., De Senneville, B.D., Moonen, C.T.W., 2003. A fast calculation method for magnetic field inhomogeneity due to an arbitrary distribution of bulk susceptibility. Concepts Magn. Reson. Part B Mag. Reson. Eng. 19B, 26–34.

Schafer, A., Wharton, S., Gowland, P., Bowtell, R., 2009. Using magnetic field simulation to study susceptibility-related phase contrast in gradient echo MRI. Neuroimage 48, 126–137.

Shmueli, K., de Zwart, J.A., van Gelderen, P., Li, T.Q., Dodd, S.J., Duyn, J.H., 2009. Magnetic susceptibility mapping of brain tissue in vivo using MRI phase data. Magn. Reson. Med. 62, 1510–1522.

Szumowski, J., Bas, E., Gaarder, K., Schwarz, E., Erdogmus, D., Hayflick, S., 2010. Measurement of brain iron distribution in Hallevorden–Spatz syndrome. J. Magn. Reson. Imaging 31, 482–489.

Wang, Y., Yu, Y., Li, D., Bae, K.T., Brown, J.J., Lin, W., Haacke, E.M., 2000. Artery and vein separation using susceptibility-dependent phase in contrast-enhanced MRA. J. Magn. Reson. Imaging 12, 661–670.

Wharton, S., Bowtell, R., 2010. Whole-brain susceptibility mapping at high field: a comparison of multiple- and single-orientation methods. Neuroimage 53, 515–525.

Wharton, S., Schafer, A., Bowtell, R., 2010. Susceptibility mapping in the human brain using threshold-based k-space division. Magn. Reson. Med. 63, 1292–1304.

Xu, X., Wang, Q., Zhang, M., 2008. Age, gender, and hemispheric differences in iron deposition in the human brain: an in vivo MRI study. Neuroimage 40, 35–42.

Yao, B., Li, T.Q., Gelderen, P., Shmueli, K., de Zwart, J.A., Duyn, J.H., 2009. Susceptibility contrast in high field MRI of human brain as a function of tissue iron content. Neuroimage 44, 1259–1266.

Zhang, J.Q., Zhang, Y.L., Wang, J., Cai, P., Luo, C.X., Qian, Z.M., Dai, Y.M., Feng, H., 2010. Characterizing iron deposition in Parkinson's disease using susceptibility-weighted imaging: an in vivo MR study. Brain Res. 1330, 124–130.

Zhu, W.Z., Zhong, W.D., Wang, W., Zhan, C.J., Wang, C.Y., Qi, J.P., Wang, J.Z., Lei, T., 2009. Quantitative MR phase-corrected imaging to investigate increased brain iron deposition of patients with Alzheimer disease. Radiology 253, 497–504.

Zivadinov, R., Schirda, C., Dwyer, M.G., Haacke, M.E., Weinstock-Guttman, B., Menegatti, E., Heininen-Brown, M., Magnano, C., Malagoni, A.M., Wack, D.S., Hojnacki, D., Kennedy, C., Carl, E., Bergsland, N., Hussein, S., Poloni, G., Bartolomei, I., Salvi, F., Zamboni, P., 2010. Chronic cerebrospinal venous insufficiency and iron deposition on susceptibility-weighted imaging in patients with multiple sclerosis: a pilot case-control study. Int. Angiol. 29, 158–175.